


Article

Quantitative Study of the Maceral Groups of Laminae Based on Support Vector Machine

Yuanzhe Wu ^{1,2} , Yunpeng Fan ^{1,2}, Yan Liu ^{1,2,*}, Kewen Li ^{3,4}, Tingxiang Zeng ^{1,2}, Yong Ma ³, Yongjing Tian ¹, Yaohui Xu ^{1,2}, Zhigang Wen ^{1,2}, Xiaomin Xie ^{1,2}  and Juan Teng ^{1,2}

¹ Hubei Key Laboratory of Petroleum Geochemistry and Environment, Yangtze University, Wuhan 430100, China

² College of Resources and Environment, Yangtze University, Wuhan 430100, China

³ State Key Laboratory of Petroleum Resources and Prospecting, China University of Petroleum, Beijing 102249, China

⁴ Guangdong Association of Circular Economy and Resources Comprehensive Utilization, Guangzhou 510095, China

* Correspondence: 500954@yangtzeu.edu.cn

Featured Application: Using Support Vector Machine identified the macerals in the laminae.

Abstract: Identifying organic matter in laminae is fundamental to petroleum geology; however, many factors restrict manual quantification. Therefore, computer recognition is an appropriate method for accurately identifying microscopic components. In this study, we used support vector machine (SVM) to classify the preprocessed photomicrographs into seven categories: pyrite, amorphous organic matter, mineral matter, alginite, sporinite, vitrinite, and inertinite. Then, we performed a statistical analysis of the classification results and highlighted spatial aggregation of some categories using the kernel density estimation method. The results showed that the SVM can satisfactorily identify the macerals and minerals of the laminae, and its overall accuracy, kappa, precision, recall, and F1 are 82.86%, 0.80, 85.15%, 82.86%, and 82.75%, respectively. Statistical analyses revealed that pyrite was abundantly distributed in bright laminae; vitrinite and sporinite were abundantly distributed in dark laminae; and alginite and inertinite were equally distributed. Finally, the kernel density maps showed that all classification results, except inertinite, were characterized by aggregated distributions: pyrite with the distribution of multi-core centers, alginite, and sporinite with dotted distribution, and vitrinite with stripe distribution, respectively. This study may provide a new method to quantify the organic matter in laminae.

Keywords: macerals; laminae; organic petrology; SVM



Citation: Wu, Y.; Fan, Y.; Liu, Y.; Li, K.; Zeng, T.; Ma, Y.; Tian, Y.; Xu, Y.; Wen, Z.; Xie, X.; et al. Quantitative Study of the Maceral Groups of Laminae Based on Support Vector Machine. *Appl. Sci.* **2022**, *12*, 9046. <https://doi.org/10.3390/app12189046>

Academic Editor: Manuel Graña

Received: 22 July 2022

Accepted: 6 September 2022

Published: 8 September 2022

Publisher's Note: MDPI stays neutral with regard to jurisdictional claims in published maps and institutional affiliations.



Copyright: © 2022 by the authors. Licensee MDPI, Basel, Switzerland. This article is an open access article distributed under the terms and conditions of the Creative Commons Attribution (CC BY) license (<https://creativecommons.org/licenses/by/4.0/>).

1. Introduction

Laminae are the most minor or thinnest virgin layers of a sedimentary rock or sediments that can be distinguished [1]. The field of petroleum geology involves the identification and quantification of organic matter in laminae [2–4], widely adopting the methods used in organic petrology to identify different macerals [5,6]. The characteristics and maturity of insoluble organic matter are utilized in related research on organic matter sources, types, sedimentary environment, and resource evaluation [7–10]. However, the quantitative analysis of macerals is usually performed manually [11,12], which relies on the standards established by the International Committee for Coal and Organic Petrology [13] and American Society for Testing and Materials standard D2799-13 (2013) [14]. Furthermore, the experimenter's experience limits the accuracy of the quantitative analysis. Therefore, the analysis results may vary from specialist to specialist and do not accurately describe information on the distribution of maceral groups and minute differences in the laminae, limiting its large-scale analysis and application. In recent years, some advanced

techniques, such as the Advanced Mineral Identification and Characterization System and X-ray diffraction, can identify organic matter in source rocks. However, the focus of these techniques is on identifying the mineral composition of rocks and they cannot identify specific macerals [3,15]. Consequently, the application of new methods to quantify macerals in source rocks is urgently needed.

Previous studies have made considerable attempts to overcome the challenges related to the quantitative study of coal macerals using computer recognition techniques. In recent years, some computer scientists have utilized support vector machine (SVM), neural networks, and random forest plots to identify as well as quantify some maceral groups and mineral components [16–21]. These scholars started from the perspective of improving the accuracy of the algorithm and proposed to achieve satisfactory results. Whereas the fluorescence mode commonly used in the manual calibration of macerals was rarely mentioned in previous studies, less attention has been paid to the macerals of conventional sedimentary rocks.

In the studies of computer scientists, methods have been developed for identifying coal macerals; however, some issues need to be overcome. First and foremost, the content of organic matter in these rocks is usually below 5% [22–24], and it requires a combination of reflected-light and fluorescent-light photomicrographs to identify maceral groups [25–27]. Therefore, it may be hard to notice certain organic matters in a sample, resulting in an insufficient sample for selecting the region of interest (ROI). Second, the morphology of macerals in shale is more complex and laborious to distinguish than in coal; thus, it is difficult to calibrate certain macerals accurately. These issues undoubtedly complicate the quantification of the microscopic components in the laminae. The different combinations and content of macerals, as well as types of laminae, however, have significant effects on oil generation [3]. Due to the variation in the tiny laminae, it is complicated to describe them using conventional methods.

To tackle these issues, this study first stitched and preprocessed hundreds of microscopic images to collect photomicrographs with a large field of view and performed image enhancement to improve the accuracy of computer recognition. Second, we classified the micrographs using SVM. Furthermore, we performed a statistical analysis of the area of the classification results. Notably, this is the first attempt at using computer recognition to identify the organic matter and its small variations in the tiny laminae of shale.

Nevertheless, an interesting point has not been addressed: how to characterize the spatial distribution of macerals in the laminae with less organic matter content. Fortunately, kernel density estimation can satisfactorily resolve the concern about the spatial distribution characteristics of geographical elements. Therefore, we attempted for the first time to utilize the method to characterize the spatial distribution of macerals in the laminae. Moreover, if comprehensive geological data are available, this method can provide supporting evidence for determining the sedimentary environment of the laminae.

2. Materials

The lacustrine shale from the second member of the Kongdian Formation in Cangdong Sag was selected, which was obtained by seasonal laminations (hundreds to thousands of μm). The total organic carbon content is 8.01%, and the average vitrinite reflectance is 0.79. This sample was made according to the industry standard ISO 7404-2 (2009) [28], using an epi-illumination microscope with a $50\times$ oil immersion objective magnification. In total, over 100 reflected-light micrographs and matching fluorescent-light micrographs of the field were obtained in a JPG format. Each image had a resolution of 2748×2208 pixels.

During the study, we divided the photomicrographs into seven categories: pyrite, amorphous organic matter (AOM), mineral matter, alginite, sporinite, vitrinite, and inertinite. Most of the shale is composed of minerals, mainly pyrite, quartz, albite, etc., and a small portion is composed of organic matter. Pyrite usually has high grayness values in white reflected light mode and is spherical or filled with biological remains. Since other minerals are transparent and hard to identify under the epi-illumination microscope, we

only identified pyrite of minerals. AOM (or bituminite), alginite, as well as sporinite belong to the liptinite group, which is an active oil-bearing component of source rocks. AOM does not have a specific shape and is usually distributed in a strip. The sporinite is elongated and differs from the AOM in that it has a more defined boundary. The alginite is ellipsoidal in shape, brighter under fluorescence, and has clearer borders. Both vitrinite and inertinite are derived from higher plants, and one of the significant differences between them is that inertinite has a higher value of brightness than vitrinite in reflected white light. Figure 1 presents the typical photomicrographs of the macerals and minerals in this sample. In fluorescence mode, we can identify alginite, sporinite, and AOM easily, while vitrinite, inertinite, pyrite, and mineral matter can be shown more clearly under white reflected light mode.

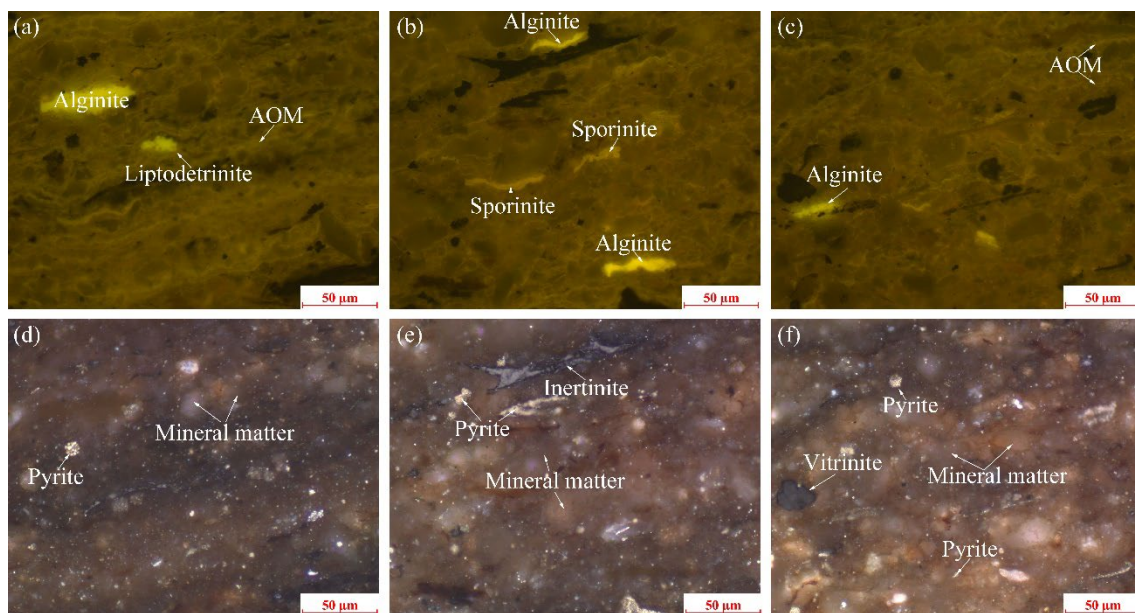


Figure 1. Illustrative examples of micrographs of macerals and minerals. (a–c) fluorescence mode; (d–f) white reflected light mode, same field as (a–c). AOM: Amorphous organic matter.

3. Methods

3.1. Software and Data Preprocessing

The software we used is the Environment for Visualizing Images (ENVI) and ArcGIS. ENVI software is widely used in remote sensing digital image processing and has also been successfully applied in other fields, such as estimating wheat crop canopy and distinguishing the shelf life of pears [29,30]. The software has the advantages of a mature algorithm, friendly interface, and convenient operation. In addition, it does not require users to have background knowledge in machine learning or program development to perform tasks such as image classification and feature information extraction. Therefore, it is highly reproducible, and we used the ENVI 5.3 software for selecting the ROI, SVM classification, accuracy check, and post classification. To facilitate the classification, we performed preprocessing, such as geometric correction, image rotation, and boundary cutting (Figure 2a,b). Owing to the stitching of photomicrographs and the small displacement of the microscope, the reflected-light and fluorescent-light images had large deviations. These differences accumulate in the large field of view images and can substantially affect the classification accuracy. As a result, we corrected the fluorescent-light micrographs using the reflected-light micrographs to erase the variations based on the nearest neighbor algorithm. We also cut boundaries to ensure that the stitched micrographs had a regular shape.

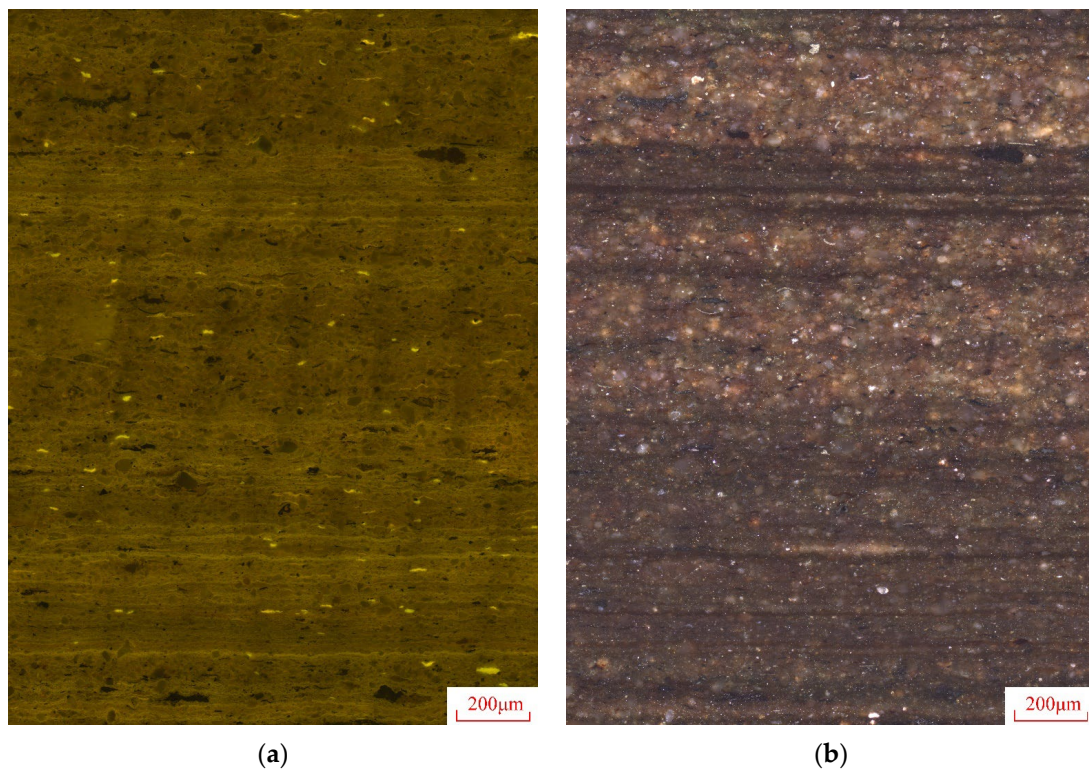


Figure 2. Data preprocessing. (a) Stitching result of geometrically corrected fluorescent-light photomicrograph; (b) stitching result of reflected-light photomicrograph.

3.2. Color Space Transformation and Feature Extraction

Compared with RGB color space, hue, saturation, and value (HSV) space has more advantages for machine learning and can better highlight the contrast level of different categories. Therefore, more scholars in image recognition use the transformation between HSV and RGB space [31,32]. Similarly, this study transformed the RGB space into HSV space to increase the accuracy of machine recognition (Figure 3).

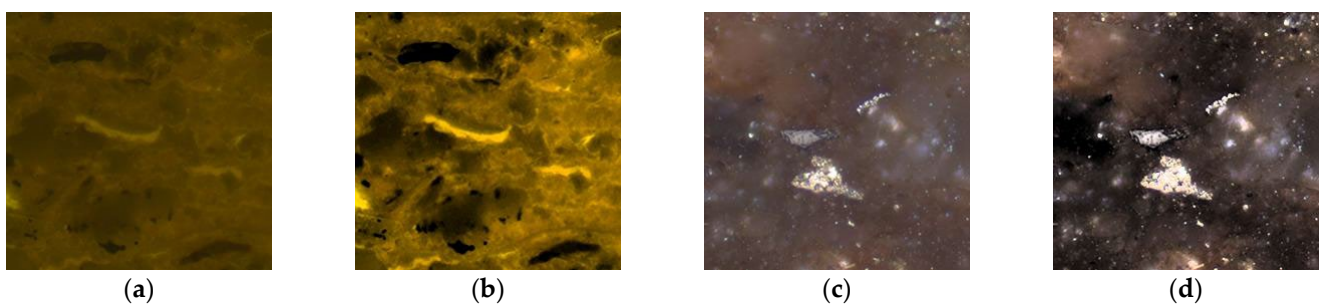


Figure 3. Color space transformation. (a) Fluorescent-light photomicrograph in RGB space; (b) fluorescent-light photomicrograph in HSV space; (c) reflected-light photomicrograph in RGB space; and (d) reflected-light photomicrograph in HSV space.

Furthermore, we analyzed eight features (mean, variance, homogeneity, contrast, dissimilarity, entropy, second moment, and correlation) based on the co-occurrence measures to extract additional photomicrograph information. Texture analysis can reflect the dispersion degree of the micrograph grayscale, distinguish macerals with similar grayscale but different internal structures, and improve the accuracy of computer recognition techniques. Since some channels have high correlation, we only performed texture analysis for fluorescent-light R and the reflected-light R channels with low correlation. As a result, the dimensionality of the dataset can be reduced as well as overfitting of the model can be avoided.

3.3. Image Classification Based on SVM

SVM is a machine learning method based on statistical learning theory that is widely used in various fields (particularly in identifying coal macerals). It can create a hyperplane, meaning an optimal separation boundary plane to minimize misclassification [33]. SVM mainly discards the training sets next to the support vectors, and the basic two-class problem in two dimensions is shown in Figure 4 [34]. This shows that even with a small training set, SVM can obtain better results in identifying microscopic components. The feature is consistent with the fact that the amount of organic matter in shale may be small. Moreover, it is a simple computational method, involving the use of few artificially set parameters [35,36]. In addition, the selection of the kernel function is critical for classification accuracy. Relying on previous experience [17,19], we used the radial basis function as the kernel function. Once the kernel function is selected, SVM has two significant parameters to determine: gamma and penalty parameter. We adopted the values automatically calculated by the software, with a gamma value of 0.05 and penalty parameter of 100. A detailed description of the SVM can be found in the papers on machine learning [34,37]. The election of ROI is also critical for machine learning, thus typical, well-characterized areas are the key ROI we chose. Through the calculation of sample separability based on the Jeffries–Matusita distance, the separability of ROI in this study was all greater than 1.97, which belonged to the qualified samples.

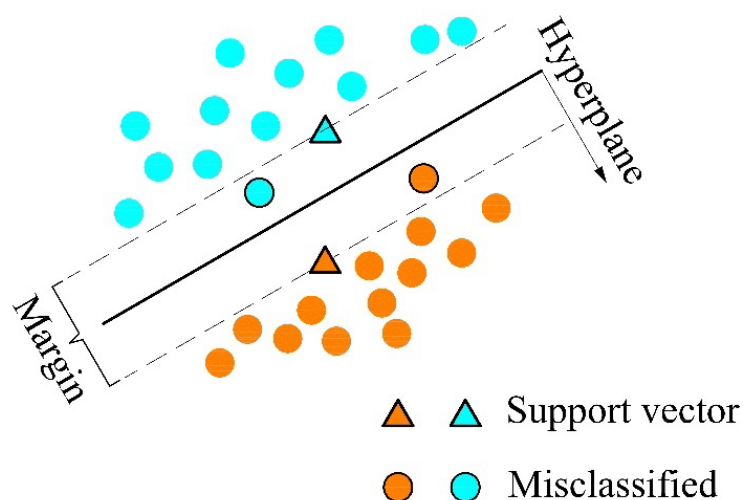


Figure 4. Example of the linear SVM. Modified from Burges (1998) [34].

After testing we found that SVM is indeed more accurate than maximum likelihood, Mahalanobis distance, and neural net among the supervised classification algorithms of ENVI (Figure 5). As a result, it is appropriate to utilize SVM for this study.

3.4. Post Classification

To improve the classification accuracy, enhance the continuity, and reduce the noise in the classified image for the following statistical analysis, a series of post-classification analyses, such as majority analysis, sieve classes, classification merging, etc., were carried out in this study. Owing to the limited resolution of the micrographs, some classification results were too small to be validated, which affected the following data analysis. Accordingly, we removed the classification results that were different from the surrounding 8 pixels and had less than 2 pixels (about 0.81 μm). We performed classification merge to classify the unclassified pixels, and these were removed by the sieve classes. In this study, we merged these pixels into mineral matter.

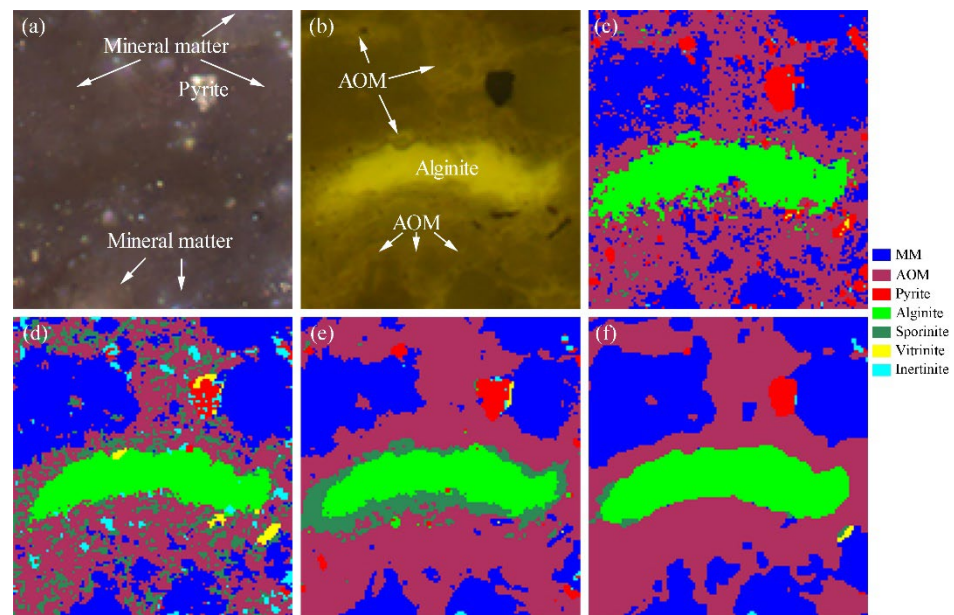


Figure 5. Examples of the results of different classification methods in the software. (a) reflected-light photomicrograph; (b) fluorescent-light photomicrograph, same field as (a); (c) maximum likelihood classification results; (d) Mahalanobis distance classification results; (e) neural net classification results; (f) SVM classification results. MM: Mineral matter.

3.5. Classification Accuracy Assessment

The kappa coefficient is an accuracy evaluation metric based on a confusion matrix and ranges from 0 to 1. The higher the value, the better the accuracy. The overall classification accuracy is the ratio of correctly classified points to the total number of points. In addition, the accuracy evaluation metrics in this study include precision (P), recall (R), and F1, which are calculated as shown in formulas (1)–(3):

$$P = \frac{TP}{TP + FP} \quad (1)$$

$$R = \frac{TP}{TP + FN} \quad (2)$$

$$F = \frac{2 \cdot P \cdot R}{P + R} \quad (3)$$

where TP, FP, and FN represent true positive, false positive, and false negative.

3.6. Statistical Analysis and Kernel Density Analysis

The area statistical analysis in this study was taken as the relative percentage content of each classification result, i.e., the percentage of each category was obtained by counting the pixel points. This can be easily achieved with the “Class Statistics” function in the ENVI software.

Kernel density estimation is a standard method that can highlight the spatial distribution characteristics of an element [38,39]. Therefore, it is also possible to show the features of maceral groups, and the higher the value, the more aggregated the distribution of macerals in the laminae. Using the ArcGIS 10.3 software, the kernel density estimation analysis was carried out by converting the feature surface data into the point data. This analysis reflects the spatial aggregation of the classification and is calculated as follows:

$$f_b(x) = \frac{1}{nh} \sum_{i=1}^n K\left(\frac{x-x_i}{h}\right) \quad (4)$$

where f_h is the kernel density value of the classifications, n is the total number of elements, h is the bandwidth, and K is the calculation function.

4. Results and Discussion

4.1. Accuracy Assessment

The classification accuracy is crucial for computer recognition. To verify the accuracy of the classification result, we first generated 350 random checkpoints using the classification result. Then, the checkpoints were modified manually according to the real macerals and minerals. Finally, the modified checkpoints were compared with the original checkpoints to derive the accuracy check metrics.

Table 1 shows the confusion matrix for the classification result, and the result of accuracy evaluation is given in Table 2. The overall accuracy, kappa, precision, recall, and F1 are 82.86%, 0.80%, 85.15%, 82.86%, and 82.75%, respectively, which meets the requirements of this study. However, some macerals and minerals are likely to be misclassified in the classification, such as inertinite misidentified as pyrite and sporinite misidentified as AOM. As a result, the precision of pyrite and AOM (76.27% and 75.81%) and the recall of inertinite and sporinite (62.00% and 70.00%) are low. In addition, the low precision of mineral matter (70.00%) is mainly because some other categories are mistakenly classified as it.

Table 1. Confusion matrix for classification result.

Categories	Pyrite	AOM	MM	Alginite	Sporinite	Vitrinite	Inertinite
Pyrite	45	0	4	0	0	0	1
AOM	0	47	1	0	1	1	0
MM	1	0	49	0	0	0	0
Alginite	0	2	5	43	0	0	0
Sporinite	0	13	1	1	35	0	0
Vitrinite	0	0	5	0	0	40	5
Inertinite	13	0	5	0	0	1	31

Table 2. Accuracy evaluation of the classification result.

Evaluation Metrics	Pyrite	AOM	MM	Alginite	Sporinite	Vitrinite	Inertinite	Overall
Precision	76.27%	75.81%	70.00%	97.73%	97.22%	95.24%	83.78%	85.15%
Recall	90.00%	94.00%	98.00%	86.00%	70.00%	80.00%	62.00%	82.86%
F1	82.57%	83.93%	81.67%	91.49%	81.39%	86.96%	71.26%	82.75%
Overall accuracy	82.86%		Kappa, K			0.80		

4.2. Image Classification Result and Statistical Analysis

Figure 6 shows the image classification result and the area percentage of each category in each lamina. The classification results can solve the challenge of quantifying macerals. Importantly, this addresses the problem that microscopic observers cannot accurately describe macerals in source rocks to other geologists.

Since mineral matter is not a maceral group and the AOM quantification criteria are controversial [40], we excluded them from the subsequent analysis. From Figure 6, it is clear that the concentrations of mineral matter and AOM are the highest. The concentrations of pyrite, alginite, sporinite, vitrinite, and inertinite in the lamina account for 1.80%, 0.39%, 0.36%, 0.59%, and 0.78% respectively (Figure 7a). However, there is a large variation in their contents in different laminae due to paleoenvironment changes [41,42]. To explore the distribution, we divided the lamina into four parts according to the differences in the brightness values [43], i.e., we labeled clayey laminae as dark laminae (dk1 and dk2), and silty laminae as bright laminae (b1 and b2).

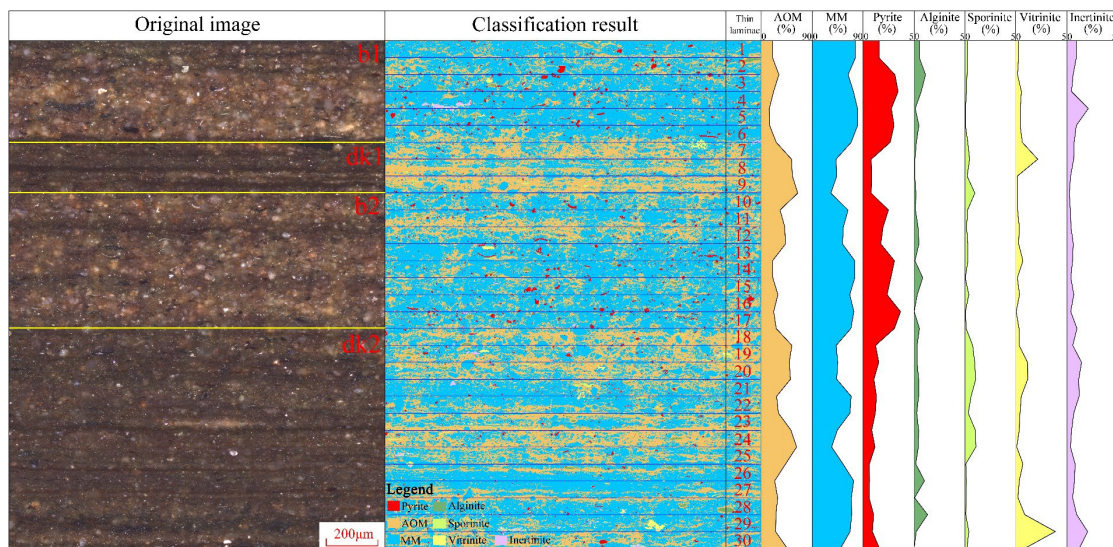


Figure 6. Image classification result and the area percentage content of each classification.

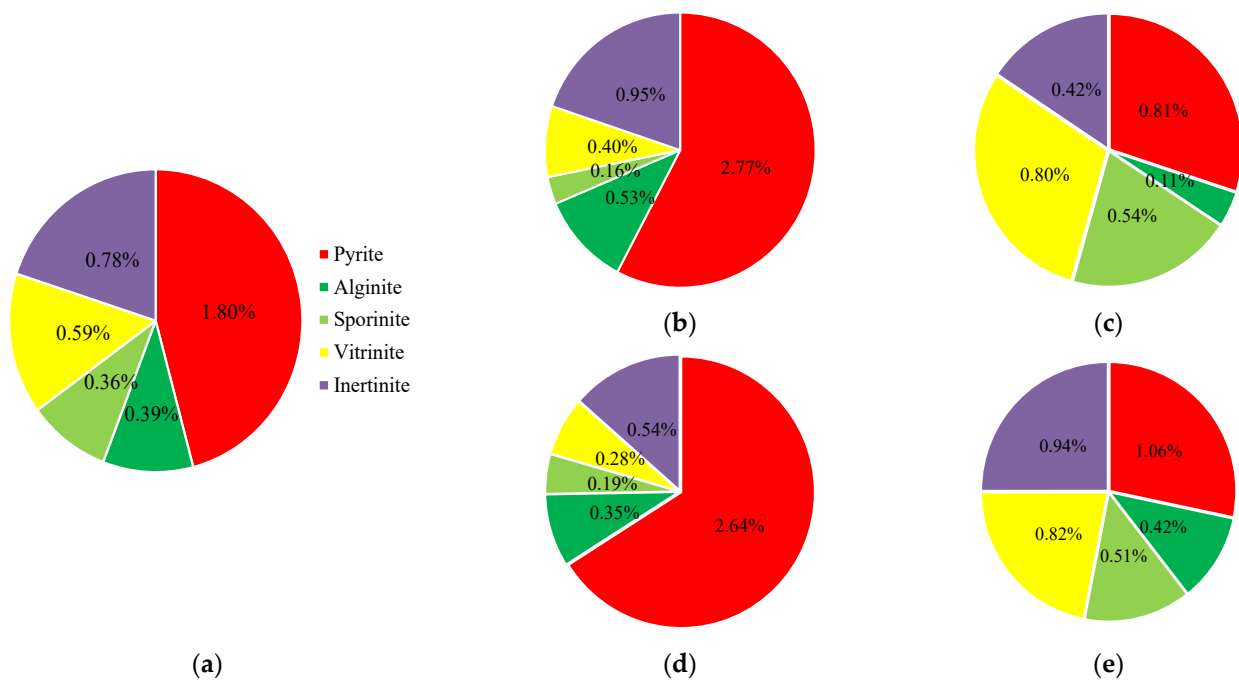


Figure 7. The area statistical analysis of image classification result. (a) Overall area proportion; (b) area proportion of b1; (c) area proportion of dk1; (d) area proportion of b2; and (e) area proportion of dk2.

In the b1 and b2 laminae (Figure 7b,d), the proportions of pyrite account for the largest area because of the extensive distribution of framboidal pyrites and the discovery of biogenic (pyrite-filled) remains in bright laminae. In the dk1 and dk2 (Figure 7c,e), vitrinite and sporinite cover the largest percentage of area. Overall, the alginite and inertinite are more equally distributed.

There are significant differences in the area ratio of the thin laminae. To further analyze the classification distribution of the results, we divided them into 30 thin laminae by pixels (Figure 6). Pyrite occupies the highest proportion in the 16th thin lamina, accounting for 3.68%, followed by 3rd and 2nd. Alginite has the highest distribution in the 28th thin lamina, namely 1.33%, followed by 2nd and 26th, with a notable variation between the 25th and 29th thin laminae. Sporinite occupies the highest proportion in the 24th thin

lamina, accounting for 1.07%, followed by 20th and 23rd. Vitrinite concentrates in the 29th, 7th, and 20th thin laminae, with the highest value being 3.86% in the 29th thin lamina. Inertinite focuses on the 4th, 29th, and 19th thin laminae, with the highest value being 2.11% in the 4th thin lamina. With this method, even tiny differences in the thin laminae can be expressed.

4.3. Analysis of the Spatial Characteristics

Although we analyzed the primary data and their variations in the laminae, the spatial aggregation characteristics cannot be highlighted. As a result, the kernel density estimation analysis was carried out to visualize the aggregation mode of each classification on the laminae. We calculated the kernel densities of pyrite, alginite, sporinite, vitrinite, and inertinite. Figure 8 shows the kernel density maps, and the spatial distribution of the components was successfully represented by this method.

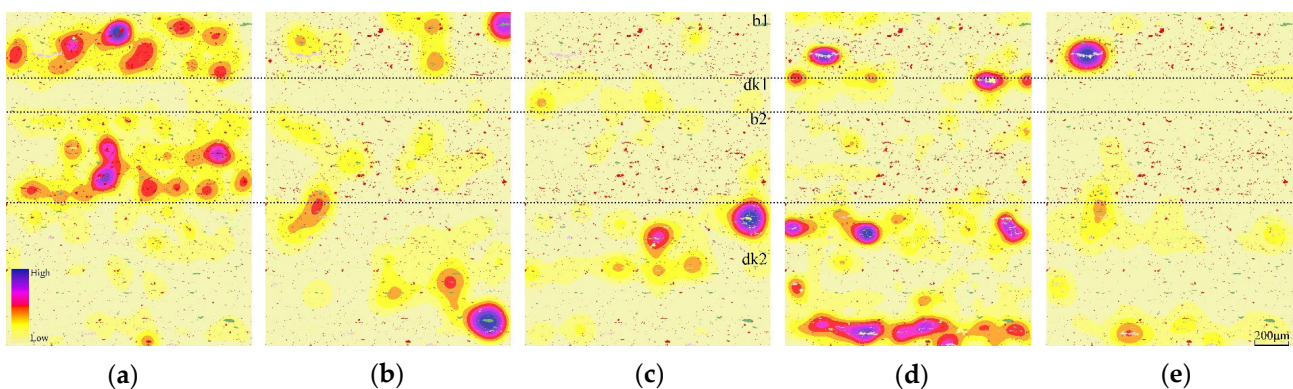


Figure 8. The kernel density maps of (a) pyrite, (b) alginite, (c) sporinite, (d) vitrinite, and (e) inertinite.

Notably, the spatial aggregations of these classifications are closely related to the four laminae (b1, dk1, b2, and dk2), divided according to the grayscale values of the reflected-light micrograph only. This indicates a pattern in the spatial distribution of microscopic components. Pyrite shows the spatial distribution of multi-core centers and is concentrated in the b1 and b2. The spatial distribution of alginite shows the dotted distribution and is concentrated in the b1 and dk2. Similarly, sporinite has the spatial distribution of dotted and is aggregated in dk2. Vitrinite is characterized by the spatial distribution of stripe and aggregated in b1 and dk2. In comparison, the aggregation distribution of the inertinite is poor. The spatial aggregation characteristics of vitrinite and inertinite have partial similarity, which may be due to misclassification.

5. Conclusions

In this study, we used SVM to quantify some maceral groups and inorganic minerals in the laminae, and the main conclusions are as follows:

- (1) Using an appropriate degree of image preprocessing and enhancement can meet geological research needs, and the overall accuracy and kappa coefficient are 82.86% and 0.80, respectively. This method is based on ENVI software and thus is replicable for geologists with little knowledge of machine learning theory. In addition, the map of classification results can illustrate the microscopic components of the source rock to other researchers.
- (2) Through statistical analysis of the classification results, it is possible to find that the organic matter and mineral areas vary in different laminae. Using this method can provide a new way for subsequent research on the combination of laminae and the difference between laminae in oil generation.

- (3) The spatial distribution of each component can be revealed by the presentation of the kernel density map: pyrite for the multi-core centers distribution, alginite and sporinite for the dotted distribution, and vitrinite for the stripe distribution, respectively; however, inertinite has no noticeable local enrichment. This discovery can assist in the follow-up study of the sedimentary environment of the laminae.

However, it is to be noted that there are some limitations in the research, which is a preliminary study of quantitative macerals in laminae. First, we performed analysis on a sample only with lamellar layers because of the lack of examples. Second, the complexity and the fewer numbers of macerals in shale led to some classification results with imperfect accuracy. Although there are limitations, this study serves to provide new approaches to quantify the macerals in laminae, and we will further investigate how to improve the accuracy of computer recognition with few samples and complex macerals in shale.

Author Contributions: Conceptualization, Y.L.; Data curation, Y.W., Y.F. and T.Z.; Formal analysis, Y.T. and X.X.; Methodology, Y.W., Y.F. and Y.L.; Project administration, Z.W.; Visualization, J.T.; Writing—original draft, Y.W.; Writing—review & editing, Y.L., K.L., Y.M. and Y.X. All authors have read and agreed to the published version of the manuscript.

Funding: This work was funded by National Natural Science Foundation of China (Grant No. 41503034, 41972122, and 42172139), National Science and Technology Major Project of China (Grant No. 2017ZX05001005-002).

Institutional Review Board Statement: Not applicable.

Informed Consent Statement: Not applicable.

Data Availability Statement: The data that support the findings of this study are openly available in zenodo.org at <https://zenodo.org/record/7049765#YxXTQHZByjg>.

Acknowledgments: We are very grateful to three anonymous reviewers for their valuable comments that improved the quality of this paper.

Conflicts of Interest: The authors declare no conflict of interest.

References

1. Hu, Q.H.; Quintero, R.P.; El-Sobky, H.F.; Kang, J.H.; Zhang, T. Coupled nano-petrophysical and organic-geochemical study of the Wolfberry Play in Howard County, Texas U.S.A. *Mar. Pet. Geol.* **2020**, *122*, 104663. [\[CrossRef\]](#)
2. Shi, Z.S.; Dong, D.Z.; Wang, H.Y.; Sun, S.S.; Wu, J. Reservoir characteristics and genetic mechanisms of gas-bearing shales with different laminae and laminae combinations: A case study of Member 1 of the Lower Silurian Longmaxi shale in Sichuan Basin, SW China. *Pet. Explor. Dev.* **2020**, *47*, 888–900. [\[CrossRef\]](#)
3. Xi, K.L.; Li, K.; Cao, Y.C.; Lin, M.R.; Niu, X.B.; Zhu, R.K.; Wei, X.Z.; You, Y.; Liang, X.W.; Feng, S.B. Laminae combination and shale oil enrichment patterns of Chang 7(3) sub-member organic-rich shales in the Triassic Yanchang Formation, Ordos Basin, NW China. *Pet. Explor. Dev.* **2020**, *47*, 1342–1353. [\[CrossRef\]](#)
4. Li, L.; Liu, Z.J.; Jiang, L.; George, S.C. Organic petrology and geochemistry of Lower Cretaceous lacustrine sediments in the Chaoyang Basin (Liaoning Province, northeast China): Influence of volcanic ash on algal productivity and oil shale formation. *Int. J. Coal Geol.* **2021**, *233*, 103653. [\[CrossRef\]](#)
5. Lin, S.H.; Yang, Z.; Hou, L.H.; Luo, X.; Liu, Q. Geostatistic recognition of genetically distinct shale facies in upper Triassic chang 7 section, the Ordos Basin, North China. *Mar. Pet. Geol.* **2019**, *102*, 176–186.
6. Lohr, C.D.; Valentine, B.J.; Hackley, P.C.; Dulong, F.T. Characterization of the unconventional Tuscaloosa marine shale reservoir in southwestern Mississippi, USA: Insights from optical and SEM petrography. *Mar. Pet. Geol.* **2020**, *121*, 104580. [\[CrossRef\]](#)
7. Luo, Q.Y.; Gong, L.; Qu, Y.S.; Zhang, K.H.; Zhang, G.L.; Wang, S.Z. The tight oil potential of the Lucaogou Formation from the southern Junggar Basin, China. *Fuel* **2018**, *234*, 858–871. [\[CrossRef\]](#)
8. Mathews, R.P.; Singh, B.D.; Singh, V.P. Evaluation of Organic Matter, Hydrocarbon Source, and Depositional Environment of Onshore Warkalli Sedimentary Sequence from Kerala-Konkan Basin, South India. *J. Geol. Soc. India.* **2018**, *92*, 407–418. [\[CrossRef\]](#)
9. Wang, S.Q.; Tang, Y.G.; Schobert, H.H.; Jiang, Y.F.; Yang, Z.D.; Zhang, X.M. Petrologic and organic geochemical characteristics of Late Permian bark coal in Mingshan coalmine, Southern China. *Mar. Pet. Geol.* **2018**, *93*, 205–217. [\[CrossRef\]](#)
10. Qiao, J.Q.; Liu, L.F.; Shang, X.Q. Deposition conditions of the Jurassic lacustrine source rocks in the East Fukang Sag, Junggar Basin, NW China: Evidence from major and trace elements. *Geol. J.* **2019**, *55*, 4936–4953. [\[CrossRef\]](#)

11. Ko, L.T.; Ruppel, S.C.; Loucks, R.G.; Hackley, P.C.; Zhang, T.W.; Shao, D.Y. Pore-types and pore-network evolution in Upper Devonian-Lower Mississippian Woodford and Mississippian Barnett mudstones: Insights from laboratory thermal maturation and organic petrology. *Int. J. Coal Geol.* **2018**, *190*, 3–28. [[CrossRef](#)]
12. Yan, Y.X.; Qi, Y.; Marshall, M.; Jackson, W.R.; Chaffee, A.L. Separation and analysis of maceral concentrates from Victorian brown coal. *Fuel* **2019**, *242*, 232–242. [[CrossRef](#)]
13. Kwiecińska, B.; Petersen, H.I. Graphite, semi-graphite, natural coke, and natural char classification—ICCP system. *Int. J. Coal Geol.* **2004**, *57*, 99–116. [[CrossRef](#)]
14. ASTM D2799-13; Standard Test Method for Microscopical Determination of the Maceral Composition of Coal. ASTM International: West Conshohocken, PA, USA, 2013.
15. Ma, W.J.; Cao, Y.C.; Xi, K.L.; Liu, K.Y.; Lin, M.R.; Liu, J.Z. Interactions between mineral evolution and organic acids dissolved in bitumen in hybrid shale system. *Int. J. Coal Geol.* **2022**, *260*, 104071. [[CrossRef](#)]
16. Mlynarczyk, M.; Skiba, M. The application of artificial intelligence for the identification of the maceral groups and mineral components of coal. *Comput. Geosci.* **2017**, *103*, 133–141. [[CrossRef](#)]
17. Wang, P.Z.; Yin, Z.H.; Wang, G.; Zhang, D.L. A classification method of vitrinite for coal macerals based on the PCA and RBF-SVM. *J. China Coal Soc.* **2017**, *42*, 977–984.
18. Skiba, M.; Mlynarczyk, M. Identification of macerals of the inertinite group using neural classifiers, based on selected textural features. *Arch. Min. Sci.* **2018**, *63*, 827–837.
19. Liu, M.; Wang, P.Z.; Chen, S.M.; Zhang, D.L. The Classification of Inertinite Macerals in Coal Based on the Multifractal Spectrum Method. *Appl. Sci.* **2019**, *9*, 5509. [[CrossRef](#)]
20. Wang, H.D.; Lei, M.; Chen, Y.L.; Li, M.; Zou, L. Intelligent Identification of Maceral Components of Coal Based on Image Segmentation and Classification. *Appl. Sci.* **2019**, *9*, 3245. [[CrossRef](#)]
21. Lei, M.; Rao, Z.Y.; Wang, H.D.; Chen, Y.L.; Zou, L.; Yu, H. Maceral groups analysis of coal based on semantic segmentation of photomicrographs via the improved U-net. *Fuel* **2021**, *294*, 120475. [[CrossRef](#)]
22. Fathy, D.; Wagreich, M.; Ntaflos, T.; Sami, M. Paleoclimatic variability in the southern Tethys, Egypt: Insights from the mineralogy and geochemistry of Upper Cretaceous lacustrine organic-rich deposits. *Cretaceous Res.* **2021**, *126*, 104880. [[CrossRef](#)]
23. Li, Y.J.; Xu, F.B.; Zeng, L.Y.; Zhang, W.J.; Li, M.L.; Liao, Y.S.; Chen, W.D. Gas source in lower Permian Maokou Formation and gas accumulation in the syncline area of eastern Sichuan basin. *J. Pet. Sci. Eng.* **2021**, *206*, 109044.
24. Omer, I.; Eswaran, P.; Ajay, M.; Jack, D. Characterization of geochemical properties and factors controlling the pore structure development of shale gas reservoirs. *J. Pet. Sci. Eng.* **2021**, *206*, 109001.
25. Gorbanenko, O.O.; Ligouis, B. Changes in optical properties of liptinite macerals from early mature to post mature stage in Posidonia Shale (Lower Toarcian, NW Germany). *Int. J. Coal Geol.* **2014**, *133*, 47–59. [[CrossRef](#)]
26. Varma, A.K.; Mishra, D.K.; Samad, S.K.; Prasad, A.K.; Panigrahi, D.C.; Mendhe, V.A.; Singh, B.D. Geochemical and organo-petrographic characterization for hydrocarbon generation from Barakar Formation in Auranga Basin, India. *Int. J. Coal Geol.* **2018**, *186*, 97–114. [[CrossRef](#)]
27. Luo, Q.Y.; Zhang, L.; Zhong, N.; Wu, J.; Goodarzi, F.; Sanei, H.; Skovsted, C.B.; Suchý, V.; Li, M.J.; Ye, X.Z.; et al. Thermal evolution behavior of the organic matter and a ray of light on the origin of vitrinite-like maceral in the Mesoproterozoic and Lower Cambrian black shales: Insights from artificial maturation. *Int. J. Coal Geol.* **2021**, *244*, 103813. [[CrossRef](#)]
28. ISO 7404-2:2009; Methods for the Petrographic Analysis of Bituminous Coal and Anthracite—Part 2: Method of Preparing Coal Samples. International Organization for Standardization: Geneva, Switzerland, 2009.
29. Banerjee, K.; Krishnan, P.; Mridha, N. Application of thermal imaging of wheat crop canopy to estimate leaf area index under different moisture stress conditions. *Biosyst. Eng.* **2018**, *166*, 13–27. [[CrossRef](#)]
30. Xiong, L.L.; Liu, Y.D.; Ouyang, A.G.; Sun, X.D.; Jiang, X.G.; Jun, H.U.; Ouyang, Y.P. Study on Non-Destructive Testing Model of Hyperspectral Imaging for Shelf Life of Crisp Pear. *Spectrosc. Spectral Anal.* **2019**, *39*, 2578–2583.
31. Kang, H.C.; Han, H.N.; Bae, H.C.; Kim, M.G.; Son, J.Y.; Kim, Y.K. HSV Color-Space-Based Automated Object Localization for Robot Grasping without Prior Knowledge. *Appl. Sci.* **2021**, *11*, 7593. [[CrossRef](#)]
32. Zhu, X.L.; Bao, W.X. Comparison of Remote Sensing Image Fusion Strategies Adopted in HSV and IHS. *J. Indian Soc. Remote Sens.* **2018**, *46*, 377–385. [[CrossRef](#)]
33. Mountrakis, G.; Im, J.; Ogole, C. Support vector machines in remote sensing: A review. *ISPRS J. Photogramm. Eng. Remote Sens.* **2010**, *66*, 247–259. [[CrossRef](#)]
34. Burges, C.J.C. A Tutorial on Support Vector Machines for Pattern Recognition. *Data Min. Knowl. Discov.* **1998**, *2*, 121–167. [[CrossRef](#)]
35. Cortes, C.; Vapnik, V. Support-vector networks. *Mach. Learn.* **1995**, *20*, 273–297. [[CrossRef](#)]
36. Vapnik, V.N. An overview of statistical learning theory. *IEEE Trans. Neural Netw.* **1999**, *10*, 988–999. [[CrossRef](#)]
37. Boser, B.E.; Guyon, I.M.; Vapnik, V.N. A training algorithm for optimal margin classifiers. In Proceedings of the Fifth Annual Workshop on Computational Learning Theory, Pittsburgh, PA, USA, 27–29 July 1992; pp. 144–152.
38. Forlin, P.; Gerrard, C.; Petley, D. Exploring representativeness and reliability for late medieval earthquakes in Europe. *Nat. Hazards* **2016**, *84*, 1625–1636. [[CrossRef](#)]
39. Zhang, Z.X.; Feng, Z.Q.; Zhang, H.Y.; Zhao, J.J.; Yu, S.; Du, W. Spatial distribution of grassland fires at the regional scale based on the MODIS active fire products. *Int. J. Wildland Fire* **2017**, *26*, 209–218. [[CrossRef](#)]

40. Teng, J.; Mastalerz, M.; Liu, B. Petrographic and chemical structure characteristics of amorphous organic matter in marine black shales: Insights from Pennsylvanian and Devonian black shales in the Illinois Basin. *Int. J. Coal Geol.* **2021**, *235*, 103676. [[CrossRef](#)]
41. Liu, C. Sedimentary environment and micro-sediment characteristics of Oligocene source rocks in Qiongdongnan Basin. *Acta Pet. Sin.* **2010**, *31*, 573–578.
42. Wu, J.; Li, H.; Goodarzi, F.; Min, X.; Cao, W.X.; Huang, L.J.; Pan, Y.Y.; Luo, Q.Y. Geochemistry and depositional environment of the Mesoproterozoic Xiamaling shales, northern North China. *J. Pet. Sci. Eng.* **2022**, *215*, 110730. [[CrossRef](#)]
43. Shi, Z.S.; Qiu, Z.; Dong, D.Z.; Lu, B.; Liang, P.P.; Zhang, M.Q. Lamina characteristics of gas-bearing shale fine-grained sediment of the Silurian Longmaxi Formation of Well Wuxi 2 in Sichuan Basin, SW China. *Pet. Explor. Dev.* **2018**, *45*, 358–368. [[CrossRef](#)]